Full Range Swept-Source Optical Coherence Tomography with Ultra Small Fiber Probes for Biomedical Imaging

Youxin Mao, Costel Flueraru and Shoude Chang
Institute for Microstructural Sciences, National Research Council Canada
1200 Montreal Rd, Ottawa, K1A 0R6, ON, Canada

1. Introduction

Optical coherence tomography (OCT) (Huang et al., 1991) is becoming an increasingly important imaging tool for many applications in biology and medicine, such as diagnosis and guided surgery. Due to its high resolution and fiber catheter capability, OCT is more attractive than current imaging technologies, such as ultrasound. An OCT system with higher sensitivity is essentially important for imaging the biomedical turbid tissue because the backscattered optical signal from the tissue is extremely weak. In the earlier stages of OCT imaging, axial (depth) ranging is provided by linearly scanned low-coherence interferometry (Youngquist et al., 1987; Takada et al., 1987). This method of OCT, referred to as time-domain OCT (TD-OCT), has a relatively slow sensitivity and imaging speed because its sensitivity is inversely proportional to the imaging speed. Fourier domain techniques in OCT have received much attention in recent years due to its significant sensitivity and speed advantages over TD-OCT (Leitgeb et al., 2003; aChoma et al., 2003; De Boer et al., 2003). Fourier domain methods include spectral-domain OCT (SD-OCT) and swept-source OCT (SS-OCT). In SD-OCT, individual spectral components of low coherence light are detected separately by the use of a spectrometer and a charge-coupled device (CCD) array (Fercher et al., 1995; Hausler & Lindner, 1998) CCD arrays however may introduce phase washout problems during the pixel integration time. Furthermore, detection using a spectrometer and CCD array cannot implement differential optical detection. SS-OCT uses a wavelength-swept laser source and photodetectors based on optical frequency-domain reflectometry for imaging (Chinn et al., 1997; aYun et al., 2003). SS-OCT is particularly important for imaging in the 1.3 µm wavelength range, where low-cost detector arrays are not available. The larger penetration depth of the OCT image by using the 1.3 µm wavelength light source is important for the biomedical turbid tissues, such as human skin and arterial plaque, in comparison to that by using 1.0 µm or shorter wavelength light source. SS-OCT could also make possible for a quadrature interferometry based on multi-port fiber couplers, for example, 3x3 quadrature interferometer (bChoma et al., 2003; aMao et al., 2008). Due to its ability to have instantaneous complex signals with stable phase information, OCT with a 3x3 quadrature interferometer could suppress the complex conjugate artifact naturally, therefore

to double the effective imaging depth. By detection of the phase from the complex signals, it also could exploit additional information of the tissue to enhance image contrast, obtain functional information, and perform quantitative measurements (Sticker et al., 2001; aZhao et la. 2000). In addition, SS-OCT could make possible for an unbalanced input fiber interferometer and differential output detection by using a Mach-Zehnder interferometer. The unbalanced input could emit larger portion of the optical power from optical source to the tissue than that to the reference mirror for increasing sensitivity (Rollins & Izatt, 1999). The differential detection is used to reduce the excess intensity noise to further sensitivity enhancement compared to SD-OCT (Podoleanu, 2000).

In SS-OCT, the location of a scatterer within tissue is obtained by a Fourier transformation of the optical measurement. When the real component of the interferometric signal is the only detected part, a complex conjugate artifact is introduced after the Fourier transformation. This artifact prevents the distinction between positive and negative object depths thereby reducing the effective imaging range by half. As imaging range is important in biomedical applications, methods for removing this complex conjugate artifact to achieve full range in SS-OCT are of significant interest. Different full-range SS-OCT imaging methods which measure the complex component of the interferometric signal by shifting the phase of the reference and/or sample reflections have been reported. This phase shift has been implemented by a high-speed electronic-optical phase modulator (Zhang et al., 2004), two high-speed acoustic-optical frequency shifters (Yun et al., 2004), and a pair of linearly polarized beams (Vakoc et al., 2006). All of these methods suffered from significant image corruption resulting from any small variations in the phase shift or birefringence of used materials. Recently, acquisition of both real and imaginary interferometric components was demonstrated using Michelson quadrature interferometers using 3x3 fused fiber couplers and non-differential optical detection (Choma et al., 2003; Sarunic et al., 2005; Sarunic et al., 2006). In reference (Sarunic et al., 2005), a 3x3 Michelson quadrature interferometer with balanced differential detection was used for acquiring the complex interferometric signal. Signal attenuation was used to achieve such balanced differential detection which resulted in loss of optical power. In this system, there was a non-complementary phase shift of 60° between the two output interferometric signals that needed to be converted to quadrature components by a trigonometric manipulation. In addition, due to the nature of the Michelson interferometer, the optical output power at one of the ports of the 3x3 coupler (1/3 of the source power) was not utilized in these references.

A wavelength-swept laser source with high-speed, high power, long coherence, i.e. narrow instantaneous linewidth, and wide sweeping range is essential for SS-OCT because the imaging speed, sensitivity, depth and resolution directly rely on the sweeping rate, output power, coherence length and sweeping range of the source. A high powered wavelength-swept laser is also needed for multi-channel SS-OCT. Much progress has been made on the development of high-speed swept lasers, but their output power has been limited. A sweeping repetition rate of 115 kHz has been demonstrated by using a 128-facet polygon scanner (Oh et al., 2005). Because the cavity length in this swept laser is not short enough, the photons do not have sufficient time within the laser cavity to build up the optical power and to narrow the linewidth through mode competition. That is why the resultant optical average power and instantaneous linewidth were low (23 mW) and wide (0.23 nm),

respectively. A better result of higher average power of 54 mW (Oh et al., 2008) has been reported, but no description of the laser system has been given. Fourier-domain mode locking (FDML) technique is an alternative approach to achieving higher sweeping speed while a higher optical power is preserved, which was reported recently (Huber et al., 2006a). An FDML wavelength-swept laser with a long cavity has a quasi-stationary operation where one wavelength propagates through the cavity and returns to an optical narrow bandpass filter. Consequently, the laser generates a sequence of narrowband optical wavelength sweeps at the cavity repetition rate. An FDML wavelength swept laser with sweeping repetition up to 370 kHz using a Fabry-Perot tunable filter has been reported (Huber et al., 2006b). Although a narrow (~ 0.1 nm) instantaneous linewidth was reached, the direct output power of this laser was low. To achieve an average output power of 36 mW at the sweeping repetition of 100 kHz, an external semiconductor optical power booster had to be used. However, an amplifier outside the cavity could cause performance degradation, e.g., an increase in linewidth (Huber et al., 2005) and system noise (Rao et al., 2007), thereby reducing the penetration depth and sensitivity of an OCT system.

In the most optically nontransparent tissues, OCT has a typical imaging depth limitation of 1-3 mm. As a result, the earliest *in vivo* OCT imaging of tissue microstructure and microvasculature was restricted to a few transparent or superficial organ sites, such as the retina (Yazdanfar et al., 2000; White et al., 2003) and skin (Zhao et al., 2000). To overcome this depth limitation, optical probes, such as endoscopes, catheters, and needles have been investigated for *in vivo* OCT imaging in mucosal layers of the gastrointestinal tract (Tran et al., 2004; Yang et al., 2005a), deep organs and tissues (Li et al., 2000; Yang et al., 2005b), and inter-arterial and intra-vascular (Fujimoto et al., 1999; Diaz-Sandoval et al., 2005). However, for the imaging of small lumen, narrow space, and deep tissue and organ of humans and small animals, a key concern is the possible damage from the mechanical insertion of the optical probe. Therefore it is critical to develop an ultra-small optical probe that is compatible with the current optical biomedical imaging systems, which results in minimum tissue damage. *In vivo* optical imaging of internal tissues is generally performed using a fiber-optic probe, since an optical fiber can be easily and cheaply produced with a diameter of less than 150 μm. The key components of such optical fiber probe include a small lens and a beam director, where both provide a focused optical beam directing it to a location of interest through a guide-wire. Traditionally, this type of small optical probe has been implemented by attaching a small radial graded refractive index (GRIN) glass rod lens or called SELFOC lens with a size range of 0.25-1.0 mm and a tiny glass micro-prism to a single mode fiber (SMF) with optical adhesive or optical epoxy (Li et al., 2000). However, the gluing of a separate small lens and a tiny prism to a fiber is a complex fabrication process that results in a low quality optical interface. A new probe design that uses optical fiber lenses, e.g., fiber GRIN lens or fiber ball lens, has been proposed (Swanson et al., 2002; Shishkov et al., 2006). The main advantage of fiber lenses over conventional glass lenses are their small size, ability to auto-align to a fiber, thus creating a fusion-spliced interface with low loss, low back-reflection, and high mechanical integrity. In addition, a beam director can be easily attached to the fiber lenses by the fusion-splice of a polished fiber spacer and direct polish on the ball lens. Beam quality of a fiber-optic probe is crucial for the imaging system. Ideal characteristics of a fiber-optic probe include a high Gaussian beam intensity profile, an appropriate intensity-distance shape, high flexibility, and low optical aberration and loss.

Swanson *et al.*and Shishkov *et al.* proposed the fiber based optic probes design, but presented the variations of probe structure instead of the characteristics of their performance (Swanson et al., 2002; Shishkov et al., 2006). Reed *et al.* demonstrated the usage of such probes with emphasis on their insertion loss only (Reed et al., 2002). Yang *et. al.* (Yang et al., 2005b), Jafri *et. al.* (Jafri et al., 2005), and Li *et. al.* (Li et al., 2006) reported OCT images without detailed characterization of the used fiber lens based probes. We recently reported design, fabrication, and characterization of the fiber probes with comparison in detail the actual optical performance of a fiber-based optic probe with modeling results (Mao et al., 2007; Mao et al., 2008).

In the second section in this chapter, we present theoretical and experimental results for a 3x3 Mach-Zehnder quadrature interferometer to acquire a complex interferometric signal for SS-OCT system. We introduce a novel unbalanced differential detection method to improve the overall utilization of optical power and provide simultaneous access to the complementary phase components of the complex interferometric signal. No calculations by trigonometric relationships are needed. We compare the performance for our setup to that of a similar interferometer with a commonly used balanced detection technique. We demonstrate complex conjugate artifact suppression of 27 dB obtained in a swept-source optical coherence tomography using our unbalanced differential detection. We show that our unbalanced differential detection has increased signal-to-noise ratio by at least 4 dB comparing to a commonly used balanced detection technique. In the third section, we demonstrate a Fourier-domain mode-lock (FDML) wavelength-swept laser based on a polygon scanner filter and a high-efficiency semiconductor optical amplifier. Peak and average output powers of 98 mW and 71 mW, respectively, have been achieved without an external amplifier, while the wavelength was swept continuously in a full wavelength of 113 nm at center wavelength of 1303 nm. A unidirectional wavelength sweeping rate of 7452 nm/ms (65.95 kHz repetition rate) was achieved by using a 72 facet polygon with a rotational rate, R, of 916 revolutions per second. The instantaneous linewidth of this laser is 0.09 nm, which corresponds to a coherence length of 16 mm. We also construct an OCT system that uses our laser source where we have shown that its parameters are optimized for this application. In the fourth section, we discuss design methods and fabrication techniques of fiber-lens-based optic probes. We compare in detail measured performance with expected theoretical performance. Finally, we demonstrate the images of human skins, animal arterial plaque and heart tissues acquired from our catheter-based complex SS-OCT, which proves our SS-OCT system with fiber catheter is most suitable for the applications of biomedical imaging.

2. Full Range (Complex) Optical Coherence Tomography System

2.1 Theoretical Analysis of the Complex System
An MZI utilizing a 3x3, two 2x2 fiber couplers, and two differential detectors is shown in Fig. 1. A 90/10 2x2 fiber coupler is used as a power divider of the light source: 90% power to the sample and 10% power to reference arms. This is an advantage of the MZI (Rollins & Izatt, 1999), which allows more light to the sample arm for compensating the lower reflection of a biological sample in an OCT system. The 3x3 fiber coupler serves not only as a combiner of the two signals from the sample and reference arms, but also provides three phase related

output interferometric signals. To form two phase related differential detections, which are necessitated to obtain the real and imaginary parts of the interferometric signal, one of the output ports of the 3x3 coupler is split using one 50/50 2x2 fiber coupler. Two differential detectors were constructed by combining one output of the 2x2 coupler and one of the remaining outputs of the 3x3 coupler. We note that the input signals for these differential detectors are not balanced, but no optical power is lost. For comparison, the different unbalanced differential detection methods with different input power ratios, achieved by adjusting two additional fiber attenuators, are also shown in Fig. 1. When the input power ratio is adjusted to achieve balanced detection (i.e. attenuation α = 0.5), the DC component of the interferometric signal could be dynamically removed, but one third of the optical power would be lost.
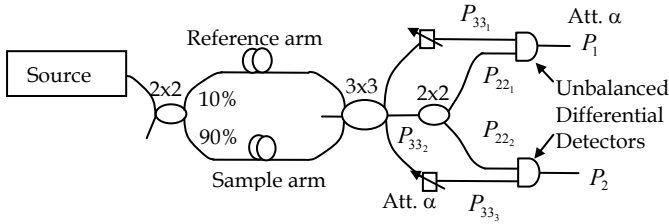

Fig. 1. Mach-Zehnder interferometer using a 3x3 and two 2x2 fiber couplers to form two channel unbalanced (attenuation α = 1 - 0.5) and balanced (attenuation α = 0.5) differential detections for acquiring real and imaginary parts of the interferometric signal.

To analyze our setup we could use transfer matrix descriptions for both 2x2 and 3x3 couplers (Sheem, 1981; Priest, 1982). The output electric field of a 2x2 coupler, $\mathbf{E}_{\mathbf{out}_{2x2}} = \begin{bmatrix} E_{out_1} & E_{out_2} \end{bmatrix}^T$, due to an input electric field, $\mathbf{E}_{\mathbf{in}_{2x2}} = \begin{bmatrix} E_{in_1} & E_{in_2} \end{bmatrix}^T$, where T denotes matrix transposition, is given by $\mathbf{E}_{\mathbf{out}_{2x2}} = \mathbf{M}_{2x2}\mathbf{E}_{\mathbf{in}_{2x2}}$, where

$$\mathbf{M}_{2x2\,50/50} = \begin{bmatrix} \sqrt{0.5} & -j\sqrt{0.5} \\ -j\sqrt{0.5} & \sqrt{0.5} \end{bmatrix} \tag{1}$$

presents the transfer matrix of a 50/50 2x2 coupler, and

$$\mathbf{M}_{2x2\,90/10} = \begin{bmatrix} \sqrt{0.9} & -j\sqrt{0.1} \\ -j\sqrt{0.1} & \sqrt{0.9} \end{bmatrix} \tag{2}$$

is the transfer matrix of a 90/10 2x2 coupler. Similarly, the output electric field of a 3x3 coupler could be written as $\mathbf{E}_{\mathbf{out}_{3x3}} = \mathbf{M}_{3x3}\mathbf{E}_{\mathbf{in}_{3x3}}$, where

$$\mathbf{M}_{3x3} = \frac{e^{-j2K_{cpl}}}{3}\begin{bmatrix} 1 & 1 & 1 \\ 1 & 1 & 1 \\ 1 & 1 & 1 \end{bmatrix} + \frac{e^{j2K_{cpl}}}{3}\begin{bmatrix} 2 & -1 & -1 \\ -1 & 2 & -1 \\ -1 & -1 & 2 \end{bmatrix} \tag{3}$$

and K_{cpl} is the coupling coefficient and equals to 0.7 for a 3x3 coupler with 1/3 power coupling ratio (Sheem, 1981).

The operation of a Mach-Zehnder interferometer could be represented by a cascade of the transfer matrices of the couplers and a matrix representing the phase shift between the

sample and reference arms ϕ. Let the input electric field and the matrix representing the phase shift between the sample and reference arms be given by $\mathbf{E_{in}} = \begin{bmatrix} 0 & 1 & 0 \end{bmatrix}^T$ and $\mathbf{M_\varphi} = \begin{bmatrix} 0 & 0 & 0 \\ 0 & 1 & 0 \\ 0 & 0 & e^{j\phi} \end{bmatrix}$, respectively. In our setup, the splitter ratio of the first 2x2 coupler is 90/10.

Therefore, the output electric field, $\mathbf{E_{33}}(\varphi) = \begin{bmatrix} E_{33_1}(\phi) & E_{33_2}(\phi) & E_{33_3}(\phi) \end{bmatrix}^T$ after the 3x3 coupler shown in Fig. 1 is calculated by:

$$\mathbf{E_{33}}(\varphi) = \mathbf{M_{3x3}}\mathbf{M_\varphi}(\phi)\mathbf{M_{2x2_{90/10}}}\mathbf{E_{in}}. \tag{4}$$

In the case of the 2x2 coupler after the 3x3 coupler, if the input electric field is given by $\mathbf{E_{in_{2x2}}}(\phi) = \begin{bmatrix} E_{33_2}(\phi) & 0 \end{bmatrix}^T$, the output electric fields, $\mathbf{E_{22_1}}, \mathbf{E_{22_2}}$, are obtained by:

$$\mathbf{E_{22_1}}(\phi) = \mathbf{M_{2x2_{50/50}}}\mathbf{E_{in_{2x2}}}(\phi), \tag{5a}$$

$$\mathbf{E_{22_2}}(\phi) = \mathbf{M_{2x2_{50/50}}}\mathbf{E_{in_{2x2}}}(\phi). \tag{5b}$$

Therefore, the related optical powers P_{33_1}, P_{22_1}, P_{22_2}, and P_{33_3} specified in Fig. 1 are calculated by:

$$P \propto \mathbf{E^*E}. \tag{6}$$

The interferometric signal powers P_1 and P_2 from the outputs of the two differential detectors v.s. the attenuation value α and the phase shift between the sample and reference arms ϕ are calculated by subtracting the two optical input signal powers of the detectors, respectively, i.e.,

$$P_1(\phi) = \alpha P_{33_1}(\phi) - P_{22_1}(\phi), \tag{7a}$$

$$P_2(\phi) = \alpha P_{33_3}(\phi) - P_{22_2}(\phi). \tag{7b}$$

The phase differences between the two interferometric signals P_1 and P_2 and the related power levels are obtained by graphing their function curves vs. ϕ.

The real (P_{RE}) and imaginary (P_{IM}) part signals, e.g. quadrature components (0° and 90°), are formed from the interferometric signals P_1 and P_2 acquired at two differential detectors using the following trigonometric equations (Choma et al., 2003):

$$P_{RE}(\phi) = P_1(\phi), \qquad P_{IM}(\phi) = \frac{P_1(\phi)\cos(\Delta\phi) - P_2(\phi)}{\sin(\Delta\phi)} \tag{8}$$

where, $\Delta\phi$ is the phase difference between the interferometric signals P_1 and P_2. The wavelength dependent power splitting ratios of the fiber couplers were neglected in this work for simplicity. SS-OCT A-scans with resolved complex conjugate artifact were obtained by inverse Fourier transformation (IFT) of the complex signal $P_{RE}+jP_{IM}$.
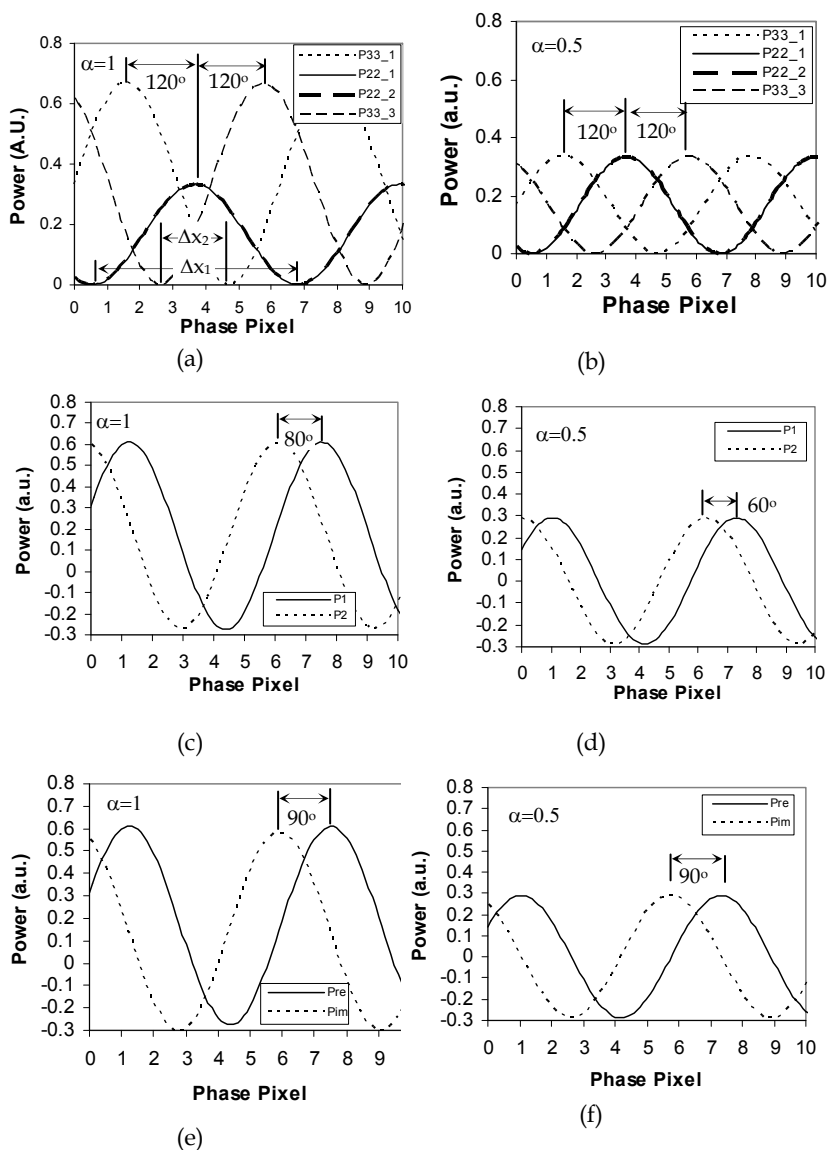
Fig. 2. Theoretical waveforms before (a, b) and after (c, d) the differential detection and after the quadrature signal calculations (e, f) when the attenuation α = 1 (a, c, e) and 0.5 (b, d, f), where α = 1.0 and 0.5 correspond to the unbalanced by a factor of 2 and balanced configurations, respectively.

Fig. 2 shows theoretical waveforms when the attenuation α = 1 (a, c, e) and 0.5 (b, d, f), where α = 1.0 and 0.5 correspond to the unbalanced by a factor of 2 and balanced

configurations, respectively. The waveforms shown in Fig.2 (a, b) and (c, d) are calculated before and after the differential detections, respectively, while the waveforms shown in Fig.2 (e, f) are calculated using the Eq. 8. The phase difference Δ was calculated using $\Delta = 2\pi\Delta x_2/\Delta x_1$, where Δx_1 and Δx_2 are the phase pixel intervals of a period and a difference of the two signals, respectively, as illustrated in Fig. 2 (a). The phase differences of 120⁰ between the two input detector signals were obtained for both α = 0.5 and 1.0 configurations as shown in Fig. 2 (a, b). This is due to the phase difference resulting from the 3x3 coupler. Because of the power difference of the input signals, the amplitude levels and the phase relationships of the output signals would be different in the two setups as shown in Fig. 2.
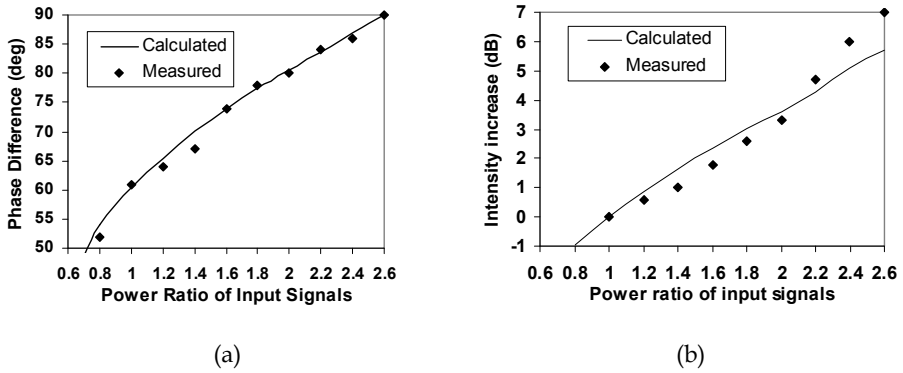
Fig. 3. Theoretical phase difference (a) and intensity increase (b) of the output signals for the unbalanced configuration from the balanced configuration verses power ratio of the two detector input signals, respectively. The experimental results are shown as the points.

Fig. 3 (a) and (b) show theoretical and experimental results of the phase difference and intensity increase of the output signals, P_1 and P_2 for the unbalanced configuration from the balanced configuration versus input power ratios of the detectors, respectively. The phase differences of the output signals are 60⁰ and 80⁰ when power ratios of input signals are 1 (balanced configuration) and 2 (unbalanced configuration), respectively, obtained both in theory and experiment. The intensities of the output signals increase 3dB when the power ratio of input signals is 2 (unbalanced configuration) comparing to the power ratio of input signals is 1 (balanced situation). The input power ratios from 2 to 2.6 for the detectors could be obtained when the coupling ratio of 3x3 was not exactly 1/3. From the results shown in Fig. 3 (a), a 90⁰ phase difference between the detector outputs P_1 and P_2 could be obtained if the input power ratio was 2.6, therefore, no calculations by the trigonometric relationships are needed for obtaining the quadrature signals.

2.2 Method of the Complex OCT System

Fig. 4 shows the experimental setup of the instantaneous complex conjugate resolved swept-source OCT system using the 3x3 Mach-Zehnder interferometer topology with the unbalanced (no attenuators) and balanced (with attenuators) differential detection schemes. The system consisted of a 2x2 single-mode fiber coupler with 90/10 coupling ratio as the

input coupler and a 3x3 fiber coupler with coupling ratios of 0.39/0.29/0.32, a 50/50 2x2 fiber couplers and two variable fiber attenuators as the output couplers forming the dual-channel balanced detection.
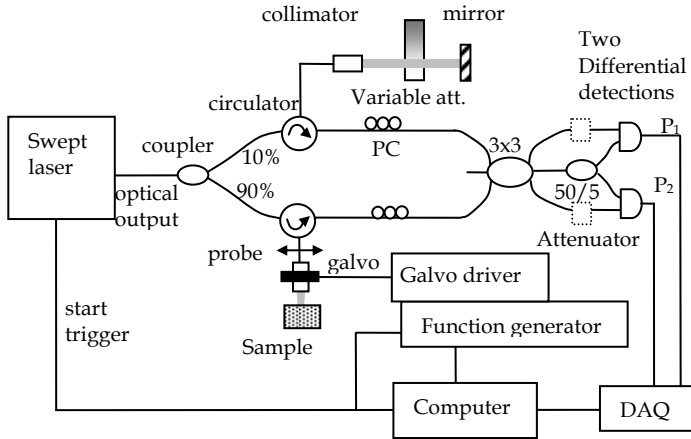

Fig. 4. Schematic diagram of the instantaneous complex conjugate resolved swept-source OCT system using the 3x3 Mach-Zehnder interferometer (MZI) topology with unbalanced (no attenuators) and balanced (with attenuators in the doted line) differential schemes. The coupler ratios of the 3x3 coupler are 0.39/0.29/0.32.

The swept source (HSL2000-HL, Santac) used in the system had a central wavelength of 1320 nm and a full scan wavelength range of 110 nm, which was sweeping linearly with optical frequency with a linearity of 0.2%. The average output power and coherence length of the swept source was 12 mW and 10 mm, respectively. A repetition scan rate of 20 kHz was used in our system and the related duty cycle was 68%. The output light from the swept laser source was launched into the first coupler and then divided into the sample arm with 90% power and reference arm with 10% power by two fiber circulators. The reference arm was arranged with a fiber collimator and a mirror. A variable attenuator was inserted between the collimator and mirror for adjusting the optical power on reference arm to achieve the higher sensitivity. The light was illuminated to a sample through the lensed single mode fiber probe with working distance (focus distance to lens surface in air) of 1.1 mm, depth of field (twice the Rayleigh range in air) of 1.1 mm, and $1/e^2$ spot diameter (transverse resolution) of 27 μm which will be described in the third section in this chapter. A galvanometer (Blue Hill Optical technologies) scanner scanned the fiber probe light transversely on the sample up to 4 mm at 20 Hz with 1000 transverse pixels. The total optical power illuminating on the sample was approximately 10 mW. Two polarization controllers (PC) in both reference and sample arms were used for adjustment to match the polarization state of the two arms. The two-pair output signals from the output couplers were detected with two-pair photodiodes to obtain quadrature signals. Two differential photo-detectors (PDB150C, Thorlabs) were used with adjustable bandwidth. A 3 dB

bandwidth of 50 MHz was used in our system. The two detector outputs were digitized using a data acquisition card (DAQ) (PCI 5122, National Instruments) with 14-bit resolution and acquired at a sampling speed of *100 MS/s*. The swept source generated a start trigger signal that was used to initiate the function generator for the galvo scanner and initiate the data acquisition process for each A-scan. Because the swept source was linearly swept with wave-number k, A-scans data with resolved complex conjugate artifact were obtained by a direct inverse Fourier transformation (IFT) from direct DAQ sampling data without any re-sampling process.

2.3 Results and Discussion of Complex OCT system

The performance of the complex conjugate ambiguity resolution in our 3x3 Mach-Zehnder SS-OCT system with the unbalanced configuration could be quantified by comparing the complex conjugate resolved A-scans with the unresolved A-scans. Measurements were taken using a -55dB reflector including coupling loss in the sample arm as shown in Fig. 4. The reference mirror was adjusted to a position such that the difference in optical path length between the two interferometer arms was 500 μm. The extra background noise was subtracted by measuring the reference arm signals with the sample arm blocked.
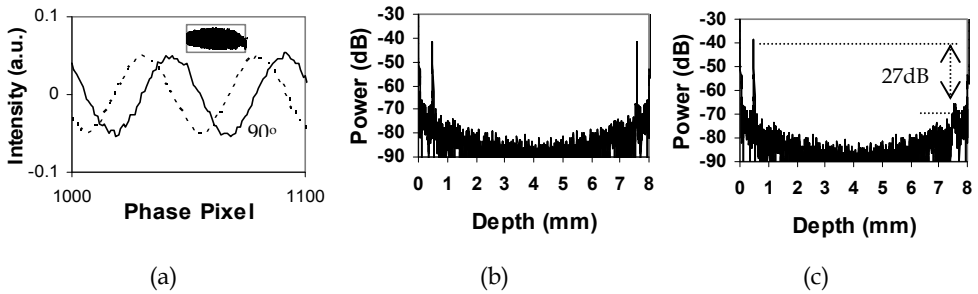

| (a) | (b) | (c) |

Fig. 5. The experimental results of the complex conjugate artifact resolution with our 3x3 MZI SS-OCT in the unbalanced differential detection with 3x3 coupler ratio of 0.39/0.29/0.32 in 500 μm path length difference of the sample and reference arms. (a): Measured interferometric signals of the output P_1 and P_2 on two detectors with phase shift of 90°. Inset: Measured full interferometric signals of the output P_1 and P_2. (b): A-scan signals obtained by IFT from a single detector include the complex conjugate artifacts. (c): A-scan signals obtained by IFT directly from the output signals at the two detectors with suppressions of the complex conjugate peaks of 27 dB.

Fig. 5 (a) shows measured waveforms of the output signal P_1 and P_2 from our unbalanced SS-OCT system with 3x3 port configuration as coupler ratio of 0.39/0.29/0.32, i.e., we connected the lowest power port of the 3x3 coupler to the 2x2 coupler. The input power ratios in this unbalanced setup were 2.8 and 2.4 for the two detectors, respectively. We noticed from the full interferometric signals of the output P_1 and P_2 shown in the inset of the Fig. 5 (a) that the DC values of the waveforms in the unbalanced system were removed by the high-pass filter of the detectors. Because a phase difference of 90° between the interferometric signals P_1 and P_2 was obtained, the data of measured P_1 and P_2 was automatically become quadrature signals. Therefore, a minimized complex conjugate

artifact was obtained after performing a complex Fourier transform operation directly from the two outputs. Fig. 5 (b) shows the A-scan at 500 μm depth obtained by inverse Fourier transform of a single detector include the complex conjugate artifact. The symmetric reflective peaks were in both positive and negative sides. Fig. 5 (c) shows the complex conjugate resolved A-scan obtained by taking the inverse Fourier transform directly from the output quadrature signals P_1 and P_2. SNR and suppression of the complex conjugate peaks of 52 dB and 27 dB was obtained at about 500 μm depths in our unbalanced differential detection SS-OCT system when the 55dB reflector in the sample arm was used. Therefore, the measured sensitivity of 107 dB was obtained in our system. We found the sensitivity obtained from the system with the unbalanced configuration was increased by 4 dB compared to the system with the balanced configuration. This is due to better utilization of optical power with our unbalanced differential detection technique.
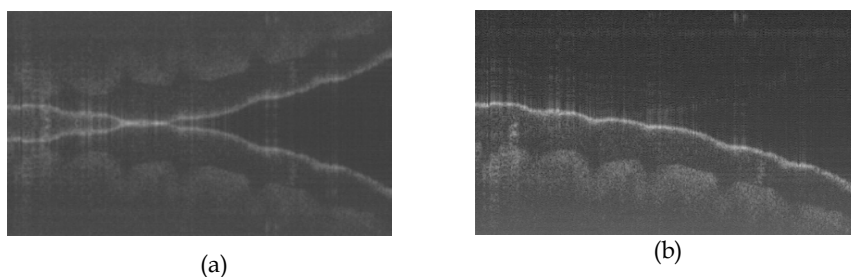

(a)   (b)

Fig. 6. *In vivo* images of human finger tip acquired by our full range swept-source optical coherence tomography using the 3x3 Mach-Zehnder interferometer with unbalanced differential detection technique. (a): the image was generated using only a single detector. (b): the complex signals were used.

Fig. 6 shows *in vivo* images of a human finger tip acquired by our full range swept-source optical coherence tomography using the 3x3 Mach-Zehnder interferometer with unbalanced differential detection technique. The resolutions of the axial and lateral are 10 μm and 27 μm, respectively. The pixel size of the images is 800x900 in correspond to the image size of 3x4mm. In Fig. 6 (a), the image was generated using only a single detector, and demonstrates the folded artifact images. In Fig. 6 (b), the complex signal was used demonstrating artifact-free imaging over a depth range of 3 mm.

3. High Performance Wavelength-Swept Laser for Optical Coherence Tomography

3.1 Optical Filter Design for Swept Laser
Fig. 7 shows a schematic diagram of the FDML wavelength swept laser with a long fiber ring cavity. A SOA is used as the gain medium in the ring cavity which has a central wavelength of 1300 nm. The SOA is considered the most suitable gain medium for OCT applications: high small-signal gain, broadband gain spectra, and high relaxation resonance frequencies. The wavelength selection was achieved by a polygon-based high-speed narrowband optical scanning filter. The unidirectional wavelength sweep of a polygon

scanner, as opposed to the inherently bidirectional Fabry-Perot filter, is better matched to the gain properties of an SOA. A mode-locked laser resonator was implemented using a long single mode fiber (SMF). The polygon-based reflection-type scanning narrow-bandpass filter (Yun et al., 2003) includes an optical fiber collimator, an optical diffraction grating, an afocal telescope, a polygon scanner, and a planar mirror. A collimated Gaussian beam with a broad optical spectrum from the SOA was first spread by the optical grating and then converged to the polygon by the telescope. The telescope, made of two achromatic doublets, controls both the beam size and angles. A planar mirror was placed after the polygon to reflect only the spectral component with normal incidence to the fiber. We note that the sweeping angle of the intermediate reflection from the polygon facet doubles the polygon's effective rotation angle, so that the free spectral range (FSR) of this filter is twice than when the polygon simply retro-reflects the light back to the telescope. The orientation of the grating incidence angle and the rotation direction of the polygon facet determine the direction of the wavelength tuning. The arrangement in Fig. 7 produced a unidirectional increase of the wavelength that resulted in higher optical power output. An optical fiber circulator was used to couple the light between the ring cavity and the filter. Three fiber polarization controllers were placed before the SOA, the circulator and the grating to optimize their polarization, respectively (Mao et al., 2009). The CW wavelength-swept light was coupled out of the cavity by a fiber coupler positioned after the SOA.
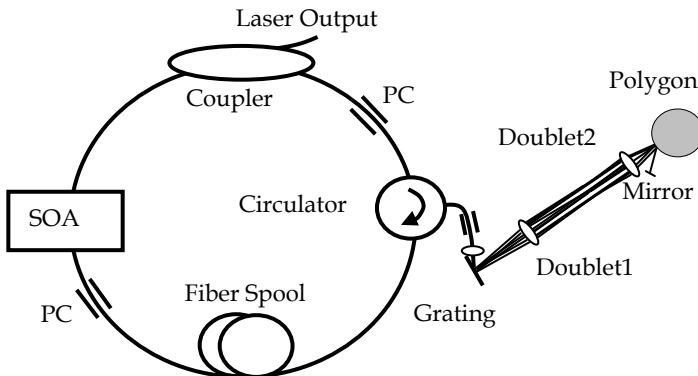

Fig. 7. Schematic diagram of a FDML wavelength-swept laser shown with a ZEMAX ray-tracing of the polygon-based narrow-band filter.

The parameters of the polygon scanning filter and its components were investigated by using a commercial optical modeling software ZEMAX (ZEMAX Development Corp., WA, USA). The ray-tracing layout of the optical filter is shown in Fig. 7 where a non-sequential ZEMAX component was used to model the polygon scanner. As the polygon was rotated clockwise by one facet, one full cycle of the continuous spectrum was swept. To achieve an optical filter with a FWHM linewidth of 0.16 nm, central wavelength of 1305 nm, free spectral range (FSR) of 110 nm, 100% duty cycle, minimum beam clipping and maximum coupling efficiency, the following optical components were chosen: a fiber collimator with 10 mm focal length and $1/e^2$ beam width of 1.89 mm, a grating with a groove frequency of 830/mm and an incident angle of 69°, two achromatic doublets with focal lengths of 75 mm

and 40 mm, a polygon scanner with 72 facets and a facet area of 6.35x2.77 mm² (Mao et al., 2009). A summary of the input parameters and simulation results are listed in Table 1. The observed 0.5 mm chromatic focal shift after F1 on both end of the spectrum wavelength ends were compensated for our double-pass arrangement. A change of the focal spot at the image plane from circular to elliptical at the edge wavelengths, shown in Fig. 8, resulted in a nearly Gaussian output spectrum due to lower coupling efficiencies at those edges.

Input Parameter	Value	Simulation Result	Value
Center wavelength	1305 nm	Collimate beam width ($1/e^2$)	1.89 mm
Input fiber, core & NA	Single mode 9 μm & 0.11	Spectral sweeping range	± 55 nm
Collimate lens	f = 10 mm ϕ = 6mm	FWHM bandwidth at central	0.16 nm
Grating density incidence angle	830g/mm ϕ=69 deg	Diverging angle after grating at 1250 and 1360nm to central	-2.637° +2.656°
Doublet 1	$F1$ = 75 mm ϕ= 25.4mm	Converging angle at polygon at 1250 and 1360nm to central	+4.944° -4.979°
Doublet 2	$F2$ = 40 mm ϕ= 25.4mm	$1/e^2$ Beam width at Polygon	2.78 mm
Polygon facet number	72	Chromatic focal shift after F1 at 1250 and 1360nm to central	0.50 mm 0.51 mm
Polygon angle per facet	5°	Image chromatic focal shift at 1250 and 1360nm to central	< 0.1 mm < 0.1 mm
Polygon radius	31.75 mm	Image spot size at 1250, 1305, and 1360nm	120 x 10 μm² 2.6 x 2.6 μm² 110 x 9 μm²
Polygon facet area	6.35x2.77mm²	Coupling efficiency at 1250, 1305, and 1360nm	7% 38% 8%

Table 1. The parameters of the polygon scanning filter obtained from ZEMAX simulation.
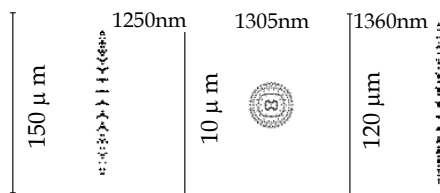

Fig. 8. Imaging spot size at 1250 nm (left), 1305 nm (central), and 1360 nm (right) of the filter from ZEMAX simulation.

The diffraction grating equation is given by (Hecht, 1979), λ = (sin α + sin β)/T, where λ is the wavelength, T is the groove frequency, and α and β are the incident and the diffracted

angles of the beam, respectively, with respect to the normal axis of the grating. The sweeping wavelength ($d\lambda$) could be expressed as (Yun et al., 2003):

$$d\lambda = (1/T)\cos\beta_0 (F_2/F_1)d\theta \tag{9}$$

where $d\theta$ is the sweeping angle of the polygon scanner and β_0 is the angle between the optical axis of the telescope and the grating's normal. Since $d\theta = 2\pi R dt$ for a polygon scanner, we could get a linear relationship between the sweeping wavelength and the sweeping time by integrating Eq. (9):

$$\lambda(t) = \lambda_1 + \frac{4\pi\cos\beta_0 F_2 R}{TF_1}t \tag{10}$$

Our design results in a wavelength sweeping rate of 7.31 mm/s.

3.2 Swept Laser Construction

A Fourier-domain mode-lock wavelength-swept laser based on polygon scanning filter and semiconductor optical amplifier was constructed. A high efficiency InP/InGaAsP quantum well SOA (BOA 1132, Covega) was used as the laser gain medium with a saturation output power of 19 dBm, small signal gain of 30 dB and FWHM bandwidth of 93 nm. The material structure of the quantum well active region of the SOA was optimized to increase the output power and bandwidth. A 72-facet polygon scanner (SA34, Lincoln Laser) that optimized for ultra-high speed stability was used. Two achromatic doublets (AC254-C, Thorlabs) were used to construct the telescope system. A 3.1 km optical fiber was inserted into a 5.1 m ring laser cavity as a delay line fiber to synchronize a repetition rate of 65.95 kHz of the polygon filter, which corresponds to a round-trip propagation time in the cavity of 15.16 μs. Using this setup, we could alternate between mode-locked and short cavity laser operation. In the mode-locked configuration, we used standard single mode fiber with zero dispersion around 1300 nm (SMF-130V, Prime Optical Fiber Corporation). The maximum mismatches in the roundtrip times of the different wavelengths due to dispersion and fiber birefringence were 1.1 ns and 0.4 ps, respectively. These values were calculated using a dispersion coefficient of 3.1 $ps\ km^{-1}\ nm^{-1}$ and polarization mode dispersion coefficient of 0.2 $ps\ km^{-1/2}$ of the used SMF-130V fiber. Therefore, these small time mismatches could be neglected. Three fiber polarization controllers for individually aligning polarization states of SOA, fiber circulator and grating were found to be necessary for obtaining maximum optical power. A fiber spool with 6 inch mandrel size was used in the cavity for the 3.1 km long SMF. We noticed that a fiber spool with 3 inch mandrel could reduce the optical power and flutter the laser spectrum, resulting in a reduction of the 3 dB bandwidth. This spectral fluctuation could be due to the inconsistent birefringence caused by the small bending radius of the long fiber. The ratio of the output coupler of 60/40 was used (60% of the power is coupled out), which was optimized to get the maximum optical output power.

3.3 Results and Discussions of the Swept Laser

The time-averaged normalized spectrum emitted from our FDML swept laser, measured by an optical spectrum analyzer (OSA) in peak-hold mode with a resolution of 1 nm, is shown in Fig. 9 (a). On the same graph we show a fitting of the measured spectrum to a Gaussian function, dashed line, and the spectrum obtained by ZEMAX simulations, dotted line. This

simulated spectrum is the product of the filter spectrum (due to different filter coupling efficiencies at different wavelengths) and the spontaneous emission spectrum of the used SOA. A full sweeping wavelength range of 113 nm and FWHM bandwidth of 90 nm at central wavelength of 1303 nm measured from our swept laser were obtained. We note that the shape of the measured spectrum is close to a Gaussian distribution. This bandwidth of the swept laser would correspond to 8.3 µm axial resolution in the air in OCT. The measured sweeping FWHM bandwidth of the FDML swept laser was 1.43 times higher than the simulated spectrum. This increase in bandwidth is due to higher optical gains in the smaller signal range at the edge wavelengths than the central wavelength. While keeping the polygon static, two spectra were measured using the highest resolution of the OSA (0.01 nm) at the center wavelength of 1303 nm and at the dual-edge wavelengths of 1248.0 nm and 1358.2 nm, shown in Fig. 9 (b) in addition to the dynamic spectrum for comparison. A distance of 110.2 nm between the two simultaneous existing peaks corresponds to the FSR of the filter, which is in good agreement with the design specifications of FSR of 110 nm. We also note that the static spectra of our FDML swept laser had a FWHM linewidth of 0.015 nm at the central wavelength as shown in the inset of the Fig. 9 (b). The measured filter linewidth was 0.17 nm at the same wavelength as shown in the Fig. 9 (c). We found the measured laser linewidth was 11.3 times smaller than that of the filter. The linewidth of filter in the edge wavelength range increased which could be caused by the off-axis effect of the doublet; however, this effect was diminished by the FDML method as shown in Fig. (c). Fig. 9 (d) shows average output power of the swept laser versus the injection current of the SOA, which shows the laser threshold current is 100 mA.
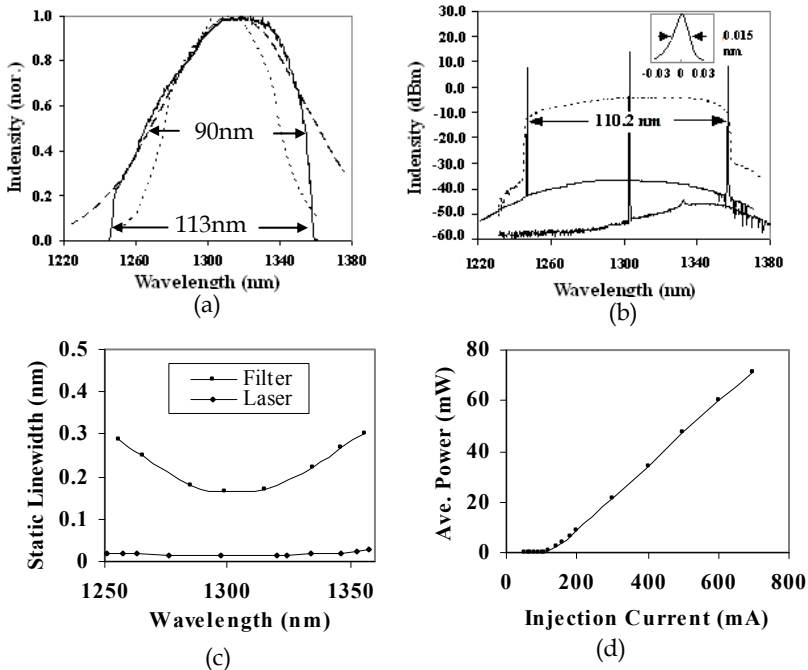

Fig. 9. (a) Measured normalized spectra of our FDML wavelength-swept laser in solid line, a

Gaussian fitting in dashed line, and simulated spectrum in dotted line. (b) Measured spectra in dBm scale with two static spectra while keeping polygon stay at the center wavelength of 1303 nm and the dual-edge wavelengths of 1248.0 nm and 1358.2 nm in solid lines. Inlet: the linear static spectrum at 1303 nm. (c) Measured static linewidth of the FDML swept-laser in comparison with measured linewidth of the polygon filter. (d) Output power versus injection current of the SOA.
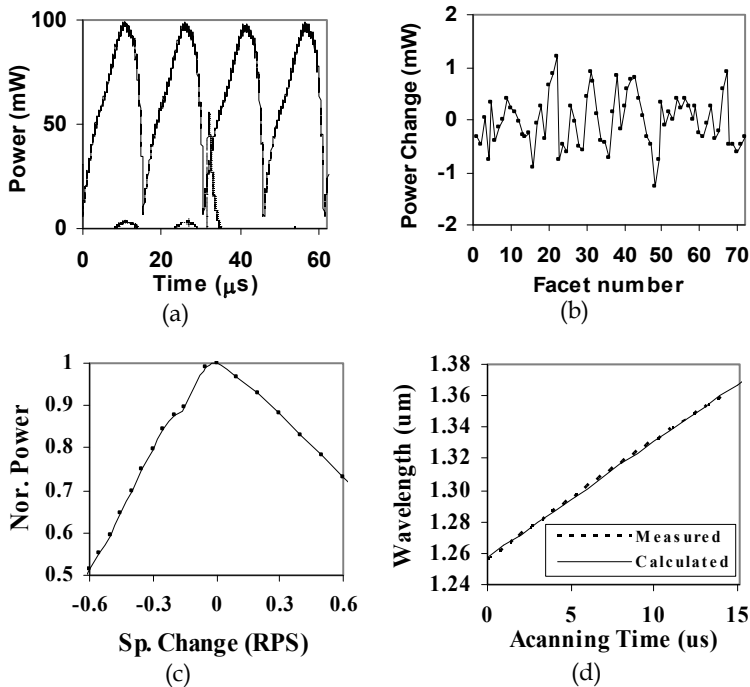

Fig. 10. (a) Oscilloscope trace of the swept laser output with four tuning cycles at a repetition rate of 65.95 kHz in solid line and a start trigger signal in dashed line. (b) Optical power change versus facet number of the polygon. (c) The normalized output power as a function of polygon speed change. (d) Theoretical and experimental wavelength swept versus time.

Fig. 10 (a) shows the measured output power of our FDML swept laser over four wavelength scans using an oscilloscope. The peak power and the average power emitted by the laser were 98 mW and 71 mW, respectively, corresponding to an SOA injection current of 700 mA. The observed scan duration of 15.16 μs with a duty cycle of 100% correspond to a repetition rate of 65.95 kHz. A wavelength start trigger signal obtained by a fiber Bragg grating (FBG) is shown in Fig. 10 (a) in dashed line, which is used for wavelength calibration and system start trigger. It will be discussed below. Laser output power change with 72 successive cycle scans were measured as shown in Fig. 10 (b). The maximum optical power change is less than 3 mW, which corresponds to a maximum 3.3% optical power fluctuation from facet to facet. Fig. 10 (c) shows the measured normalized output power of the laser as a

function of the polygon rotation speed change. For this measurement, a function generator was used as an external driver to the polygon scanner. The change in the rotation speed of the polygon was obtained by adjusting the output voltage of the function generator. The laser output power was reduced when the scanner speed was either increased or decreased from the specific speed of 916 revolutions per second (RPS). More power reduction was observed when the polygon speed decreased than when it increased. This effect could be caused by the nonlinearities of semiconductor optical amplifier (Bilenca, 2006). Because the speed stability of our polygon is less than 0.02%, i.e., the speed fluctuation is less than ± 0.1 RPS, the fluctuation in the measured output power caused by the variation of the polygon speed was less than 1.0%.
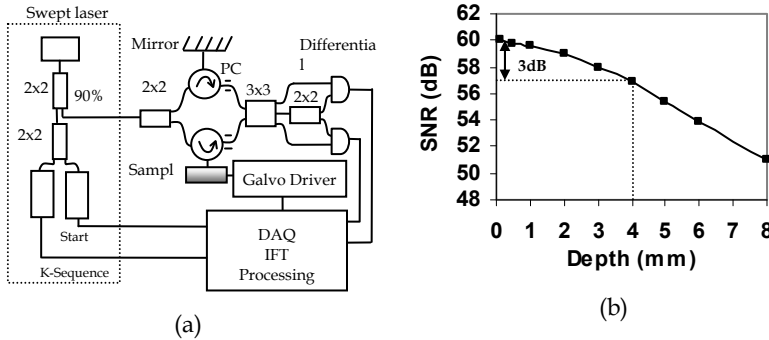

(a)

(b)

Fig. 11. (a) Schematic diagram of a complex OCT system using our swept laser with the start trigger and k-sequence. (b) The SNR of the OCT system with out swept source in the different depths.

To further characterize the properties of our swept laser for OCT application, 10% of the output power of the laser was connected to a 2x2 coupler to obtain a trigger corresponding to the start wavelength, λ_1, and a sequence of equal differences in the propagation constant k, $\Delta k = 2\pi\Delta\lambda/\lambda^2$, where $\Delta\lambda$ is the difference in wavelength. This sequence of equal valual of k is called a *k-sequence*. The start wavelength trigger for the wavelength calibration was implemented using a fiber Bragg grating with central wavelength of 1256 nm and bandwidth of 0.3 nm, a fiber circulator, and a photo-detector. The sharp rising edge of the start trigger as shown in Fig. 10 (a) in dashed line was used for the trigger of the data acquisition and wavelength calibration in the OCT system. The *k-sequence* was generated using a Mach-Zhender interferometer (MZI) with an adjustable optical path length difference and a balanced detector. By adjusting the optical path difference to about 8 mm, 1024 peaks at equal values of k were obtained. The measured wavelengths of these 1024 peaks, where Δk is equal, versus times was shown in Fig. 10 (d). We found that the measured results were in good agreement with the theoretical results calculated from Eq. 10. Using the remaining 90% of the optical output power of our swept source, we constructed a complex OCT system using a 3x3 MZI as described in the section 2 and shown in Fig. 11 (a). Measurements at different object depths were taken using a mirror and an attenuator in the sample arm. The extra background noise was subtracted by measuring the reference arm signals with the sample arm blocked. The complex interferometric signals were digitized by

a data acquisition card (ATS-460, AlazarTech) with 14-bit resolution and acquired at a sampling speed of *125MS/s*. The signal data with equal-k interval were obtained by an interpolation. The start trigger signal was used to initiate the *k-sequence* and the data acquisition process for each A-scan. A-scans with resolved complex conjugate artifact were obtained by a complex inverse Fourier transformation (IFT). The signal noise ratio (SNR) versus depth was obtained by measuring point spread functions (PSF) in the different depth as shown in Fig.11 (b). PSF has a FWHM value of 8.8 μm, which agrees well with the 8.3 μm equivalent to the 3 dB bandwidth of the spectrum of the laser source. Maximum sensitivity of 114 dB was obtained by adding the attenuation in the sample arm to the SNR. To estimate the dynamic coherence length of this swept source, we observed a 3 dB drop in the amplitude of the PSF when the arm length difference was about 4 mm as shown in Fig. 11 (b). This result corresponds to an optical coherence length of 16 mm or a linewidth of 0.09 nm. We also observed a drop of 9 dB in the amplitude of the PSF at an object depth of 8 mm.

Cavity Length	3100 m (FDML)	5.1 m short cavity		
Repetition Rate (kHz)	65.95	21.5	43.8	62.1
FWHM Bandwidth (nm)	90	84.6	79.0	71.4
Coherence Length (mm)	16	14	12	10
Average Power (mW)	71	62	50	42

Table 2. Comparison of the performance of our FDML laser with 5.1m short cavity laser

To get a better understanding of the operation of our FDML swept laser, we switched the laser to the shorter cavity. Table 2 shows a comparison of the FWHM spectral bandwidth, instantaneous coherence length and average output power of our FDML swept laser operating at 65.95 kHz repetition rate to that of the short cavity swept laser operating at 21.5 kHz, 43.8 kHz, and 62.1 kHz repetition rates, respectively. In this short cavity laser, when the repetition rate increases, the laser performance is deteriorated, for example, when the repetition rate increases from 21.5 kHz to 62.1 kHz, the FWHM spectral bandwidth, instantaneous coherence length and average output power decreases from 84.6 to 71.4 nm, 14 to 10 mm, and 62 mW to 42 mW, respectively. In comparison, the FWHM bandwidth, coherence length, and average output power of our FDML swept laser reaches 90 nm, 16 mm, and 71 mW at 65.95 kHz repetition rate, respectively. From these results, the FDML technique in the swept laser source has proved to be an effective method for enhancing the overall performance of the swept laser.

4. Fiber Probes for Optical Coherence Tomography Imaging

4.1 Design of fiber probes
Fiber-based OCT system has capability of using an optic fiber probe. The light beam usually is guided through a SMF and is focused on a tested sample by an optical lens attached to the SMF. Back-reflected light carrying information about the sample is coupled back into the fiber, and then signal detection and data processing systems will collect the useful information for imaging. The optic probe is one of the crucial parts of OCT imaging system. The beam profile, i.e. working distance (focal distance from lens surface), depth of field (two times the Raleigh range), and spot size (waist diameter) of the optical probe in the sample

will directly determine the properties of the image such as image location, depth, and resolution. Thus, image quality and light coupling efficiency from the sample will be directly influenced by the beam quality of the probe. For the best optical performance of a probing lens, its beam profile must be designed to be consistent with the light penetration depth in the sample. In most biomedical imaging systems, light from the probe will be directed into a turbid tissue. Based on interaction properties of light with turbid tissue (Sainter et al., 2002) the range of penetration depth is from 0.5-3 mm at near infrared wavelengths. For example, the penetration depths are 0.7 mm and 3.0 mm in human skin and liver respectively at 1300 nm, a conventional wavelength used in OCT systems. Thus, for designing an optical probe, working distance should be in the range of 0.4 – 1.2 mm in the air that depends on the tissues to be tested. There is a tradeoff between the depth of field and beam spot size because the depth of field of a lens is positively related to the square of the spot size according to the theory of Gaussian beam. A large depth of field unavoidable results in a large spot size. Thus, the optimal depth of field is in the range of 0.8 - 1.5 mm in the air; this keeps the spot size in the range of 26 - 35 μm at the 1300 nm wavelength. For an ultra-small optical lens, it is not possible to achieve a large working distance by directly attaching a lens to a SMF because of the strong focus ability of lens and the small mode field diameter (MFD) of the SMF. A fiber spacer with a homogeneous index of refraction has to be added between the SMF and the lens for beam expansion prior to focusing to obtain a larger working distance. Therefore, theoretical modeling becomes necessary to obtain a fiber lens with optimized optical beam performance for imaging different tissues.

In this section, we study two types of fiber lenses, GRIN and ball fiber lenses. We used ZEMAX to design both GRIN and ball fiber lenses by choosing an appropriate surface type and analysis method.
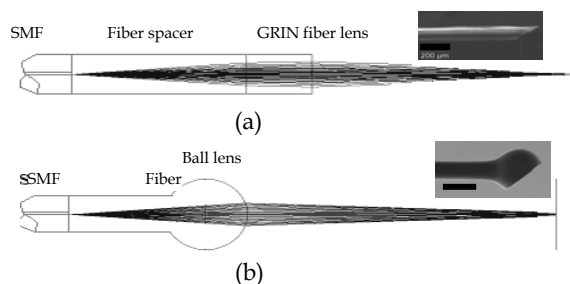

Fig. 12. ZEMAX layouts of ray trace for the GRIN (a) and ball (b) fiber lens systems, respectively. Insets: scanning electron micrographs of the GRIN and ball fiber lens tips fused with angle-polished beam director, respectively. Marks are 200 μm.

For a GRIN fiber lens, the gradient surface type used in ZEMAX will depend on the profile of the refractive index. The refractive index profile of the GRIN fiber lens used in this work is a radial index gradient, which is very similar to that of a conventional glass GRIN (or called SELFOC) lens. The index of refraction is highest in the center of the lens and decreases with radial distance from the axis. The following quadratic equation closely describes the refractive index of a GRIN fiber lens (Kogelnik & Li, 1966; Emkey & Jack, 1987):

$$n(r) = n_0(1 - \frac{g^2}{2}r^2)$$ (11)

where r is the radial position from the axis, n_0 is refractive index on the lens axis, g is the gradient constant. The pitch, $p = 2\pi/g$, is the spatial period of the ray trajectory. For modeling of the ball fiber, the Standard Surface type in ZEMAX is employed. Fig. 12 (a) and (b) show the ZEMAX ray trace layout of the GRIN and ball fiber lenses, respectively, with their scanning electron micrographs in the insets. The working distance, depth of field and spot size were calculated in ZEMAX using the Gaussian beam theory. The theoretical results will be shown and discussed in comparison with the experimental results below.

4.2 Fabrication Method of the fiber probes

The GRIN and ball fiber lens probes were made from a standard Corning SMF-28 single mode fiber as the principal light guide, a fiber spacer and a GRIN or a ball fiber lens as the focusing lens. For the GRIN lens probe, a fiber spacer with same outer diameter (0.125 mm) as SMF-28 was fusion-spliced via arc welds to the Corning SMF-28 and then accurately cleaved to a theoretically-determined length. A GRIN fiber was then fusion-spliced to the cleaved fiber spacer and precisely cleaved at a pre-calculated length to generate a desired beam-distance profile (i.e., working distance, depth of field, and spot size). For a short working distance probe, the section of the fiber spacer was omitted resulting in a simple fabrication process. For the ball lens probe, a fiber spacer was fusion-spliced via arc welds to the Corning SMF-28 and then accurately cleaved to a theoretically-determined length plus extra 0.2 mm. The tip of the fiber spacer then was fused via arc welds to a perfect ball shape by inputting an appropriate fusion setting. To ensure minimum back-reflection for both probes, the indexes of the fiber spacer and the center of GRIN fiber were matched to the core index of the SMF.

We used a conventional low cost off-the-shelf optical multi-mode GRIN fibers as the GRIN lens, which has 0.1 mm core size, 0.14 mm outer diameter, a core refractive index $n_0 = 1.487$, and a gradient constant $g = 3.76$ at 1300 nm (Prime Optical Fiber Corp., Taiwan). The fiber spacers (Prime Optical Fiber Corp., Taiwan) are made of pure silica without a core. Fusion-splicing was processed using an Ericsson FSU 995 fusion-splicer and an EFC11 fiber cleaver (3SAE Technologies, TN, USA). The spliced interfaces produced minimum back-reflections since the mechanical strength at the interface was similar to that of the untreated fiber. The desired focused beam profile was obtained by tailoring the length of the fiber spacer and parameters of fiber lenses (length of GRIN fiber and diameter of the ball) based on the theoretical results. We fabricated the different variations of the GRIN and ball fiber lens modules with the different length of the fiber spacer and the different lens parameter. All samples were listed in Table 3 with detailed information.

A beam profile measurement system (BeamView Analyzer, OR, USA) with an infrared camera (Electrophysics, NJ, USA) and a Super Luminous Diode source (Covega, MD, USA) with 60nm 3dB bandwidth at 1310 nm center wavelength was used to characterize the beam parameters of the lens system. A 40X JIS microscopic objective lens and a related objective tube were attached to the input window of the camera to increase the image resolution. The horizontal and vertical resolutions of the system were 1.0 μm and 1.1 μm, respectively. The

distribution of light intensity at various distances along the direction of propagation after the lens was accurately measured by the beam profile system. Working distance, depth of focus, $1/e^2$ spot size, and Gaussian fitting were analyzed from the measured intensity distribution. The results demonstrated in this work are all in the air medium.

In addition, after characterization of the lens, a beam director could be attached to the lens for a side-view probe. The different attaching methods were used for the two lenses. For the GRIN lens, a fiber spacer was fusion-spliced to the finished lens end as a beam director by polishing the end of the fiber spacer to a 45 degrees angle and coating the polished surface with a total reflection film. This then allowed the beam to be reflected at a 90 degrees angle creating a side-view probe. For the ball lens probe, the beam can be 90-110 degree reflected by a 45-50 degree polished face on the ball lens by the total internal reflection. Insets of Fig. 12 (a) and (b) show the typical scan electron microscope (SEM) pictures of the GRIN and ball fiber lens tip fused with beam directors, respectively. The fiber lens tip together with a tubing system and a connected linearly scanning or 360 degrees rotated motor could be built as an endoscope, or catheter, or a needle probes. The diameter of these probes could be as small as 0.4 mm which is best suitable for internal *in situ* and *in vivo* biomedical imaging, diagnostic, guided surgery, and treatment with a minimal invasion.
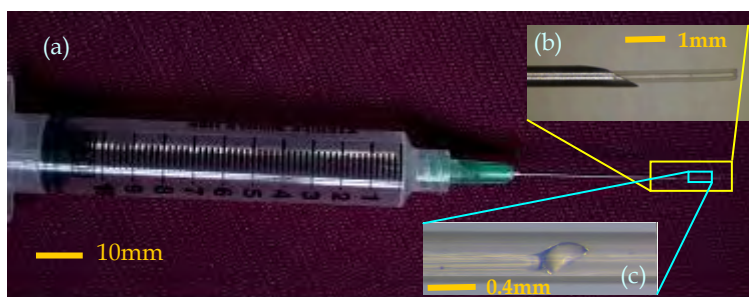

Fig. 13. OCT side-view needle probe showing the tubing and angle-polished ball lens. (a) needle probe. (b) retracted needle tip with protective tubing. (c) protective tubing and exposing the lens.

As a sample, a needle probe designed for the OCT imaging in this work is shown in Fig 13 (a). The lens and the uncoated portion of the SMF are protected in a transparent inner catheter (OD 0.49 mm) shown in Fig. 13 (b, c). The buffered portion of the fiber is attached to an outer flexible catheter after the syringe (OD 1.4 mm), which is fastened onto a modified syringe piston, while the transparent inner catheter is inserted into a 21 G (OD 0.81 mm) echogenic spinal needle (VWR, Mississauga, ON, Canada). After insertion into the tissue, the needle can be drawn back while the optical probe stays inside of the tissue as shown in Fig. 13 (b). The probe is then scanned axially inside the tissue driven by a linear scanner, such that a two dimensional OCT image is formed. If a fiber GRIN lens is used, the size of the inner catheter could be as small as 0.4 mm because the diameter of the GRIN lens is smaller than the fiber ball lens.

Sp.#	Length of Fiber Spacer (mm)	Fiber Lens		Measured Beam Properties		
		Type/Diameter (µm)	Length (mm)	Working Distance (mm)	Depth of Field (mm)	Spot Size (µm)
1	0	GRIN100/140	0.60	0.18	0.16	13
2	0	GRIN100/140	0.55	0.20	0.30	16
3	0	GRIN100/140	0.52	0.28	0.50	22
4	0	GRIN100/140	0.50	0.38	0.60	23
5	0	GRIN100/140	0.48	0.41	0.85	25
6	0	GRIN100/140	0.46	0.40	1.30	30
7	0	GRIN100/140	0.45	0.38	1.45	32
8	0.48	GRIN100/140	0.17	1.00	0.95	28
9	0.48	GRIN100/140	0.16	1.10	1.5	35
10	0.48	GRIN100/140	0.145	1.20	1.8	41
11	0.48	GRIN100/140	0.14	1.05	2.0	45
12	0.52	Ball Lens/300	~	1.00	3.6	50
13	0.55	Ball Lens/300	~	1.4	2.1	45
14	0.62	Ball Lens/300	~	1.20	1.1	27
15	0.70	Ball Lens/300	~	1.00	0.5	20
16	0.74	Ball Lens/300	~	0.90	0.33	16

Table 3. Structures of the various fiber lenses with measured beam properties.

4.3 Characterization Results of the fiber probes

The measured results of the beam properties are listed in Table 3 along with detailed descriptions of the listed samples. For each sample, optical intensity distribution data on the radial (i.e. x and y) planes were collected along the beam propagation (i.e. optical axial z) direction from the plane of the first half peak intensity (begin-plane), through the maximum intensity plane, i.e. focus plane (center-plane), to the second half peak intensity plane (end-plane). Beam properties including working distance, spot size, and depth of field were analyzed by measured intensity distribution data with distance from the lens surface to the focal plane, $1/e^2$ beam diameter at the focal plane, and the distance between the begin-plane and the end-plane, respectively. The theoretical and experimental results of working distance, depth of focus, and spot size of different variations vs. length of GRIN fiber or diameter of the ball lens (bottom x-axis), and length of fiber spacer (top x-axis) are shown in Fig. 14 (a), (b), and (c), respectively, where, lines represent the theoretical results from ZEMAX at 1300 nm, amount them, dark doted line represent GRIN fiber lens without a fiber spacer, dark and light solid lines represent GRIN fiber lens with a constant length of fiber spacer (0.48 mm) and a constant length of GRIN fiber (0.17 mm), respectively; dark and light dash lines represent ball fiber lens with a constant length of fiber spacer (0.62 mm) and a constant diameter of the ball (0.30 mm), respectively. The experimental results were represented by points, amount them, triangle points represent GRIN fiber lens and square points represent the ball lens.

From the theoretical result shown in Fig. 14, short working distance (<0.4 mm) could be obtained by the GRIN fiber lens without fiber spacer shown as the dark dotted lines. To

obtain larger working distance, a fiber spacer has to be used. In these cases, the working distance varies sharply with the length of GRIN fiber for the GRIN fiber lens and with the diameter of the ball for the ball fiber lens, but it varies less sharply with the length of the fiber spacer. The working distances have saturated values for each case. By compensating the working distance with the depth of field and the spot size, the optimized parameters (i.e. 0.9 – 1.2 mm working distance, 0.9 – 1.1 mm depth of filed, and <30 µm spot size) are not at the position of the largest working distance, instead, the optimized positions are around 0.17 mm length of the GRIN fiber with 0.48 mm length of fiber spacer for GRIN fiber lens and 0.3 mm diameter of ball and 0.62 mm length of fiber spacer for ball fiber lens. The results of the experimental results as shown in Fig. 14 and Table 3 indicated that the ZEMAX numerical optical design software were in a good agreement with the experimental results. We obtained the working distance of 1.0 mm, the depth of field of 0.95 mm, and the spot size of 28 µm from a GRIN fiber lens module (sample #8) and the working distance of 1.2 mm, the depth of field of 1.1 mm, and the spot size of 27 µm from a ball fiber lens module (sample #14).

(a)   (b)   (c)
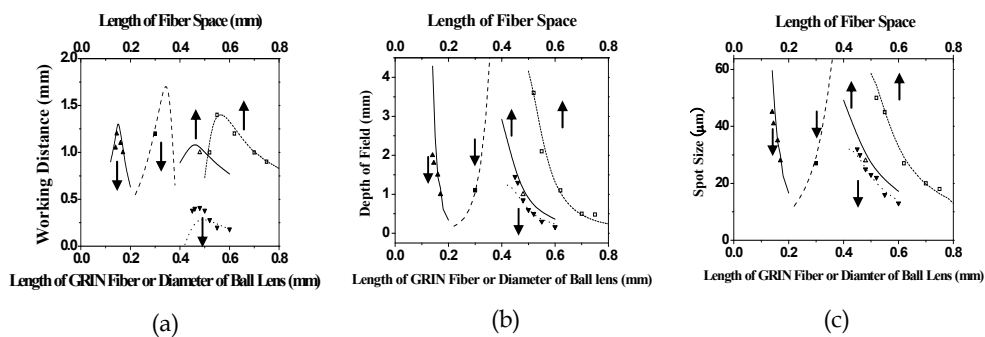
Fig. 14. Theoretical and experimental results of working distance (a), depth of field (b), and spot size (c) vs. length of GRIN fiber or diameter of the ball lens (bottom x axis), and length of fiber spacer (top x axis), where, lines represent the theoretical results from ZEMAX at 1300 nm, amount them, dark doted line represent GRIN fiber lens without a fiber spacer, dark and light solid lines represent GRIN fiber lens with a constant length of fiber spacer (0.48 mm) and a constant length of GRIN fiber (0.17 mm), respectively; dark and light dash lines represent ball fiber lens with a constant length of fiber spacer (0.62 mm) and a constant diameter of the ball (0.30 mm), respectively. The related experimental results were represented by the points.

We found quality of the beam depends very much on the quality of the surface cleaving and the alignment of the fusion-splicing between the fiber spacer and the fiber lens. The high quality beam is easier to obtain for the probe with the ball fiber lens because the ball is made from the fiber spacer and there is no interface between the fiber spacer and the ball lens. By well controlling the cleaving and the fusion-splicing, we obtained high quality of beam for the probe of the GRIN fiber lens as well. Fig. 15 shows measured and Gaussian-fitted $1/e^2$ intensity beam diameters along the axial distance z (zero is the position of the lens surface) at x (horizontal) and y (vertical) radial coordination in the distance range of depth of field for the samples #1, #3 and #8 with the GRIN fiber lenses as shown in Table 3.
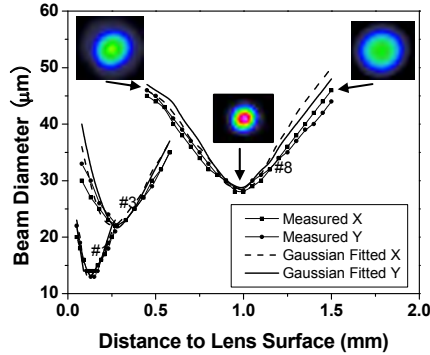
Fig. 15. Measured and Gaussian-fitted $1/e^2$ intensity beam diameters along the axial distance (zero is the position of the lens surface) at x (horizontal) and y (vertical) radial coordination in the distance range of depth of field of the samples #1, #3 and #8, which was made from the GRIN fiber lens. Insets: the cross-section beam profiles at three planes for the sample #8.

For each curve in Fig. 15, the smallest beam diameter value presents the spot size, x-coordinate value at the pole point indicates the working distance, and the distance range of the curve indicates the depth of field. The working distance of 0.18 mm, depth of field of 0.16 mm, and spot size of 13 μm were obtained for the sample #1 with 0.60 mm length of 100/140 GRIN fiber lens which was directly attached to SMF without fiber spacer. If the length of GRIN fiber was reduced to 0.52 mm, the beam became less converged resulting the three parameters increased slightly to 0.28 mm, 0.5 mm, and 22 μm, respectively. When a 0.48 mm fiber spacer was inserted between SMF and GRIN fiber and the length of GRIN fiber is reduced to 0.17 mm, significant less converged beam is observed. The working distance of 1.0 mm, depth of field of 0.95 mm, and spot size of 28 μm were obtained for sample #8.

The measured beam diameters are well matched to Gaussian-fitted values in the center (focused) regions, but have small deviations in the two edge side regions as shown in Fig. 15. The insets in Fig. 15 shown images of the cross-section beam profile at begin, center, and end planes, respectively, for the sample #8. The circular shapes of the profile images indicate high x and y symmetry of the beam profiles through all the range of depth of filed.

Considering chromatic aberrations, from ZEMAX simulation for the ball fiber lens in the wavelength range of 1260 – 1370 nm, the relative variations of the working distance, depth of field and spot size were calculated all smaller than 4.0%. For the GRIN fiber lens, the range of the zero-dispersion wavelengths, $\{\lambda_0\}$ is 1297-1316 nm. The zero-dispersion slope, S_0, equal to or smaller than 0.101 ps/nm^2-km. Using the standard formula of fiber dispersion, $D(\lambda) = S_0[\lambda - \lambda_0^4 / \lambda^3]/4$ (ps/nm-km), we calculated the changes of refractive index in the 1260 – 1370 nm wavelength range. By using these values in ZEMAX, we calculated the

relative changes of the working distance, depth of field and spot size were all smaller than 3%. Based on our results, the desired beam profile for the application of optical biomedical imaging systems can be obtained by the GRIN and ball fiber lens with or without fiber spacers. The technique described here possesses a high degree of flexibility for designing ultra-small optical probes with different beam shapes for the different tissue imaging.

5. OCT Imaging

Fig. 16 (a) and (d) show SS-OCT images of human finger *in vivo* taken using fiber probes # 14 (working distance, depth of field and spot diameter of 1.2 mm 1.1 mm, and 27 μm) and # 16 (working distance, depth of field and spot diameter of 0.9 mm 0.33 mm, and 16 μm) acquired by our catheter-based complex SS-OCT using our 3x3 Mach-Zehnder interferometer with unbalanced differential detection technique with image size of 5x2mm. The image depth shown in Fig. 16 (a) is slightly larger than that in Fig. 16 (b), but the image is blurrier in Fig. 16 (a) than that in Fig. 16 (b), which taken by the probe with larger depth of field and spot size. The image shown in Fig. 16 (b) has higher resolution than that in Fig. 16 (a), which can be seen clearly with finer structures in layer of epidermis (grey arrow), sweat gland (white arrow), and blood vessel in subcutis layer (black arrow).

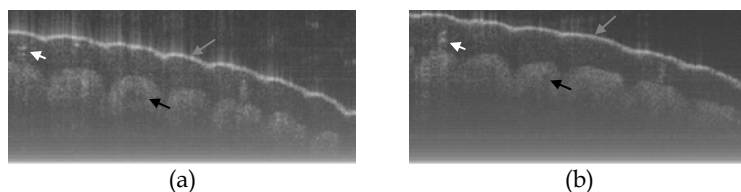(a)   (b)

Fig. 16. *In vivo* human finger SS-OCT images taken with probe #14 (working distance, depth of field and spot diameter of 1.2 mm 1.1 mm, and 27 μm) and # 16 (working distance, depth of field and spot diameter of 0.9 mm 0.33 mm, and 16 μm) acquired by our catheter-based complex SS-OCT using our 3x3 Mach-Zehnder interferometer with unbalanced differential detection technique with image size of 5x2mm.

Fig. 17 shows *ex vivo* images of coronary artery of rabbit with forward-view (a, b) probe with ball lens #16 and side-view (c, d) probe with GRIN lens #5 acquired by our catheter-based complex SS-OCT using our 3x3 Mach-Zehnder interferometer with unbalanced differential detection technique with image size of 2.5x2mm by scanning the probe along the artery (a, c) and scanning cross the artery (b, d). Three layers of tunica intima, tunica media, and tunica adventitia for the coronary artery are viewed clearly as indicated by the gray, black, and white arrows in all four images in Fig. 17. The fine layers of muscle and elastic fiber in the tunica media of the coronary artery are shown obviously in the images obtained by scanning the probe cross the artery.
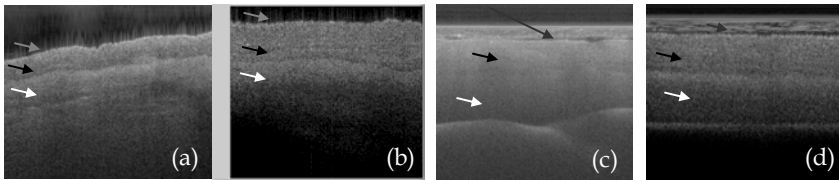
Fig. 17. *Ex vivo* images of coronary artery of rabbit scanning along the artery (a, c) and scanning cross the artery (b, d) with forward-view probe (a, b) with ball lens #16 and side-view (c, d) probe with GRIN lens #5 acquired by our catheter-based complex SS-OCT using our 3x3 Mach-Zehnder interferometer with unbalanced differential detection technique.

Fig. 18 shows *ex vivo* images of heart atrium (a, b), artery (c) of mice, and heart atrium (d, e, f) of pig with forward-view probe with ball lens #16 acquired by our catheter-based complex SS-OCT using our 3x3 Mach-Zehnder interferometer with unbalanced differential detection technique with image size of 2x2mm. The shapes and structures of these internal organs of small and large animals are viewed clearly from these OCT images.
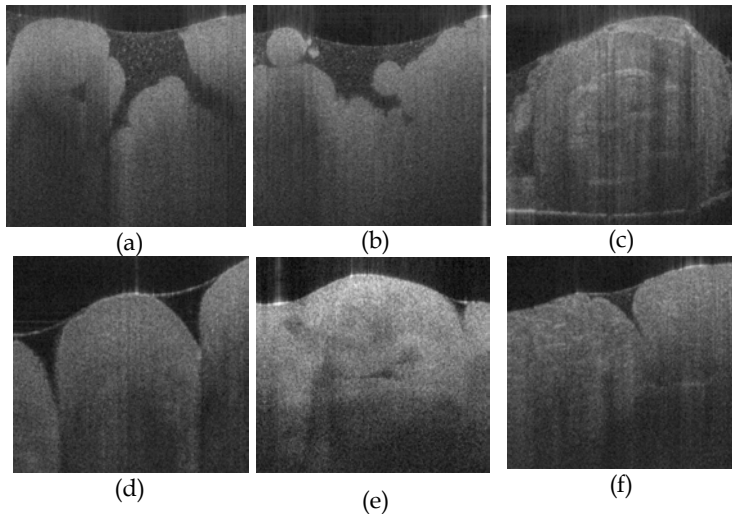

Fig. 18. *Ex vivo* images of heart atrium (a, b), artery (c) of mice, and heart atrium (d, e, f) of pig acquired by our catheter-based complex SS-OCT using our 3x3 Mach-Zehnder interferometer with unbalanced differential detection technique.

The *in vivo* and *ex vivo* OCT images shown in Fig. 16, 17, and 18 indicate that our catheter-based complex SS-OCT system is capable of imaging the biomedical tissues or the inside organs for human, small and big animals and it is most suitable for applications of diagnosis and guided surgery.

6. Acknowledgments

7. Conclusion

We have demonstrated a catheter-based full range swept-source optical coherence tomography system. A 3x3 quadrature Mach-Zehnder interferometer with a new unbalanced differential detection method for SS-OCT have been firstly presented. Using this setup, a complex conjugate artifact suppression of 27 dB has been achieved. A 90° phase shift between the two interferometric outputs was obtained thereby eliminating the need for further trigonometric calculations. Also, our setup resulted in a 4 dB increase in the signal-to-noise ratio compared to a similar interferometer with the commonly used balanced detection technique. We have then demonstrated a high-performance wavelength-swept laser that uses a high-efficiency semiconductor optical amplifier, a high-speed polygon-based narrowband scanning filter, and a Fourier domain mode lock technique. This laser produced 71 mW average output power with an instantaneous linewidth of 0.09 nm, and it could be tuned over a wavelength range of 113 nm at a repetition rate of 65.95 kHz. We also constructed an OCT system that uses our laser source where we have shown that its parameters are optimized for this application. We presented next the design, construction and beam profile characterization of different variations of graded-index and ball fiber lenses, which were recently proposed for ultra-small probes for OCT imaging. Those fiber lens modules were made of single mode fibers and GRIN and ball fiber lenses with/without fiber spacers between them. We used fusion-splicing in between the fibers, lenses and spacers to ensure high quality light transmission. We found that beam-distance profiles (i.e. 0.4 - 1.2 mm of focus distance, 0.8 – 1.5 mm of depth of field, and 26 – 35 µm of spot size) can be obtained by precisely adjusting the lengths of the fiber spacer and the GRIN fiber lens or diameter of the ball lens for the different tissue imaging in human beings and animals. We obtained very high quality focused Gaussian beam profiles with high x and y symmetry using the conventional multi-mode GRIN fibers and home-made fiber ball lenses. Their high quality beam and ultra-small size make such fiber lens based probes very valuable for biomedical optical imaging systems. The *in vivo* and *ex vivo* OCT images acquired by our catheter-based full range SS-OCT system indicate that this system is capable of imaging the biomedical tissues or inside organs for human, small/big animals and it is most suitable for applications of diagnosis and guided surgery.

8. References

Bilenca, A. et al. (2006). Numerical study of wavelength-swept semiconductor ring lasers: the role of refractive-index nonlinearities in semiconductor optical amplifier and implications for biomedical imaging application, *Opt. Lett.* 31, 760-762, ISSN: 0146-9592.

Chinn, S.R.; Swanson, E. A. & Fujimoto, J. E. (1997). Optical coherence tomography using a frequency-tunable optical source, *Opt. Lett.*, 22, 340-342, ISSN: 0146-9592.

[a]Choma, M.A. et al. (2003). Sensitivity advantage of swept source and Fourier domain optical coherence tomography, *Opt. Exp.* 11, 2183-2189, ISSN: 1094-4087.

[b]Choma, M.A.; Yang, C. & Izatt, J.A. (2003). Instantaneous quadrature low-coherence interferometry with 3x3 fiber-optic couplers, *Opt. Lett.* 28, 9672162-2164, ISSN: 0146-9592.

De Boer, J.F. et al. (2003). Improved signal-to-noise ratio in spectral-domain comared with time-domain optical coherence tomography, *Opt. Lett.* 28, 2067-2069, ISSN: 0146-9592.

Diaz-Sandoval, L. J. (2005). Optical Coherence Tomography as a tool for percutaneous coronary interventions, *Catheter. And Cardio. Interventions,* 65, 492-496, ISSN: 1522-1946.

Emkey W. L. & Jack, C. A. Analysis and evaluation of graded-index fiber-lenses, *J. of Lightwave Tech.*, LT-5, 1156-1164, ISSN:0733-8724.

Fercher, F. et al. (1995). Measurement of intraocular distances by backscattering spectral interferometry, *Opt. Commun.* 117, 443-448, ISSN: 0030-4018.

Fujimoto, J. G. et al. (1999) High resolution in vivo intra-arterial imaging with optical coherence tomography, *Heart*, 82, 128-133,.

Hausler, G. & Lindner, M. W. (1998). Coherence Radar and Spectral Radar - new tools for dermatological diagnosis, *J. Biomed. Opt.* 3, 21-31, ISSN: 1083-3668.

Hecht, E. (1997) *Opics* (Addison-Wesley, Reading, Mass.).

Huang, D. et al. (1991). Optical coherence tomography, *Science*, 254, 1178-1181, ISSN: 0036-8075.

Huber, R. et al. (2005). Amplified, frequency swept lasers for frequency domain reflectometry and OCT imaging: design and scaling principles, *Opt. Exp.*, 13, 3513-3528, ISSN: 1094-4087.

Huber, R.; Adler, D.C. & Fujimoto, J.G. (2006). Buffered Fourier domain mode locking:unidirectional swept laser sources for optical coherence tomography imaging at 370,000 lines/s, *Opt. Lett.* 31, 2975-2977, ISSN: 0146-9592.

Huber, R.; Wojtkowski, M. & Fujimoto, J.G. (2006) Fourier domain mode locking (FDML): a new laser operating regime and applications for optical coherence tomography, *Opt. Exp.* 14, 3225-3237, ISSN: 1094-4087.

Jafri, M. S. et al. (2005) Optical coherence tomography in the diagnosis and treatment of neurological disorders, *J. Biomed. Opt.* 10(5) 051603, ISSN: 1083-3668.

Kogelnik, H. W. & Li, T. (1966) Laser Beam and Resonators, *Appl. Opt.* 5, 1550, ISSN: 0003-6935.

Leitgeb, R.; Hitzenberger, C.K. & Fercher, A.F. (2003). Performance of Fourier domain vs. time domain optical coherence tomography, *Opt. Exp.* 11, 889-894, ISSN: 1094-4087.

Li, H. et al. (2006). Feasibility of interstitial doppler optical coherence tomography for in vivo detection of microvascular changes during photodynamic therapy, *Lasers in Surgery and Medicine* 38, 754–761, ISSN:0196-8092.

Li, X. et al. (2000). Imaging needle for optical coherence tomography, *Opt. Lett.* 25, 1520-1522, ISSN: 0146-9592.

Mao, Y. et al. (2007) Graded-index fiber lens proposed for ultrasmall probes used in biomedical imaging, *App. Opt.*, 46, 5887-5894, ISSN: 0003-6935.

[a]Mao, Y. et al. (2008). 3x3 Mach-Zehnder Interferometer with Unbalanced Differential Detection for Full Range Swept-Source Optical Coherence Tomography, *Appl. Opt.* 47, ISSN:2004-2010.

[b]Mao, Y. et al. (2008) Design and Implementation of Fiber Lenses for Ultra-Small Probes Used in Biomedical Imaging, *Proc. SPIE*, 6826, 68261A, ISSN: 0277-786X.

Mao, Y. et al. (2009). High Performance Wavelength-Swept Laser with Mode-Locking Technique for Optical Coherence Tomography, *Opt. Comm.*, 282, 88-92, ISSN:0030-4018.

Oh, W. Y. et al. (2005). 115 kHz tuning repetition rate ultrahigh-speed wavelength-swept semiconductor laser, *Opt. Lett.* 30, 3159-3161, ISSN: 0146-9592.

Oh, W. Y. (2008). Speed polarization sensitive optical frequency domain imaging with frequency muliplexing, *Opt. Exp.* 16, 1096-1103, ISSN: 1094-4087.

Podoleanu, A. Gh. (2000). Unbalanced versus balanced operation in an optical coherence tomography system, *Appl. Opt.* 39, 173-182, ISSN:2004-2010.

Priest, R. G. (1982) Analysis of fiber interferometer utilizing 3x3 fiber coupler, *IEEE Trans. Microwave Theory Tech*, MTT-30, 1589-1591, ISSN:0018-9480.

Rao, B. et al. (2007). Investigation of coherence amplification with a semiconductor optical amplifier employed in a swept source OCT system, *Proc. of SPIE*, 6429, 642924-1, ISSN: 0277-786X.

Reed, W. A.; Yan, M. F. & Schnitzer, M. J. (2002). Gradient-index fiber-optic microprobes for minimally invasive *in vivo* low-coherence interferometry, *Opt. Lett.* 27, 1794-1796, ISSN: 0146-9592.

Rollins, A. M. & Izatt, J. A. (1999). Optimal interferometer designs for optical coherence tomography, *Opt. Let.*, 24, 1484-1486, ISSN: 0146-9592.

Sainter, A. W.; King, T. A. & Dickinson,V Theoretical comparison of light sources for use in optical coherence tomography, *Proc. SPIE* 4619, 289-299, ISSN: 0277-786X.

Sarunic, M.V. et al. (2005). Instantaneous complex conjugate resolved spectral domain and swept-source OCT using 3x3 fiber couplers, *Opt. Exp.* 13, 957-967, ISSN:1094-4087.

Sarunic, M.V.; Applegate, B.E. & Izatt, J.A. (2006). Real-time quadrature projection complex conjugate resolved Fourier domain optical coherence tomography, *Opt. Lett.* 31, 2426-2428, ISSN: 0146-9592.

Sheem, S. K. (1981) Optical fiber interferometers with [3x3] directional couplers: analysis, *J. Appl. Phys.* 52, 3865-3872, ISSN:0021-8979.

Shishkov, M.; Bouma, B. E. & Tearney, G. J. (2006). System and method for optical coherence tomography, *U.S. Patent* 20060067620A1 (Mar. 30).

Sticker, M. et al. (2001). Quantitative differential phase measurement and imaging in transparent and turbid media by optical coherence tomography, *Opt. Lett.* 26, 114-116, ISSN: 0146-9592.

Swanson, E. (2002). Ultra-small optical probes, imaging optics, and methods for using same, *U.S. Patent* 6445939 (Sept. 3).

Takada, K. et al. (1987). New measurement system for fault location in optical waveguide devices based on an interferometric technique, *App. Opt.* 26, 1603-1606, ISSN: 0003-6935.

Tran, P. H. et al. (2004). *In vivo* endoscopic optical coherence tomography by use of a rotational microelectromechanical system probe, *Opt. Lett.* 29, 1236-1238, ISSN: 0146-9592.

Vakoc, B.J.et al. (2006) Elimination of depth degeneracy in optical frequency_domain imaging through polarization-based optical demodulation, *Opt. Lett.* 31, 362-364, ISSN: 0146-9592.

White, B. R. et al. (2003). In vivo dynamic human retinal blood flow imaging using ultra-high-speed spectral domain optical coherence tomography, *Opt. Exp.* 11, 3490-3497, ISSN: 1094-4087.

Yang, V. X. D. et al. (2005). Endoscopic Doppler optical coherence tomography in human gastrointestinal tract: initial experience, *Gastrointest. Endosc.* 61, 879-890, ISSN: 0016-5085.

Yang, V. X. D. et al. (2005). Interstitial Doppler optical coherence tomography, *Opt. Lett.* 30, 1791-1793, ISSN: 0146-9592.

Yazdanfar, S.; Rollins, A. M. & Izatt, J. A. (2000) Imaging and velocimetry of the human retinal circulation with color Doppler optical coherence tomography, *Opt. Lett.* 25, 1448-1450, ISSN: 0146-9592.

Youngquist, R. C.; Carr, S. & Davies, D. E. N. (1987). Optical coherence-domain reflectometry: A new optical evaluation technique, *Opt. Lett.*, 12, 158-160, ISSN: 0146-9592.

[a]Yun, S.H. et al. (2003). High-speed optical frequency-domain imaging, *Opt. Exp*. 11, 2953-2963, ISSN: 1094-4087.

[b]Yun, S. H. et al. (2003). High-speed wavelength-swept semiconductor laser with a polygon-scaner-based wavelength filter, *Opt. Lett.* 28, 1981-1983, ISSN: 0146-9592.

Yun, S.H. et al. (2004). Removing the depth-degeneracy in optical frequency domain imaging with frequency shifting, *Opt. Exp.* 12, 4822-4828, ISSN: 1094-4087.

Zhang, J. et al. (2004). Full range polarization-sensitive fourier domain optical coherence tomography, *Opt. Exp.* 12, 6033-6039, ISSN: 1094-4087.

[a]Zhao, Y. et al. (2000). Phase-resolved optical coherence tomography and optical Doppler tomography for imaging blood flow in human skin with fast scanning speed and high velocity sensitivity, *Opt. Lett.* 25, 114-116, ISSN: 0146-9592.

[b]Zhao, Y. et al. (2000). Doppler standard deviation imaging for clinical monitoring of *in vivo* human skin blood flow, *Opt. Lett.* 25, 1358-1360, ISSN: 0146-9592.